Electronic Supplementary Material (ESI) for Dalton Transactions.

Magnetic anisotropies of Ho(III) and Dy(III) single-molecule magnets experimentally determined via polarized neutron diffraction

Emil A. Klahn,[a] Andreas M. Thiel,[a] Rasmus B. Degn,[a] Iurii Kibalin,[c] Arsen Gukassov,[c] Claire Wilson,[b] Angelos B. Canaj,†,[b] Mark Murrie,[b*] Jacob Overgaard[a*]*

[a]Department of Chemistry, Aarhus University, DK-8000 Aarhus C, Denmark

[b]School of Chemistry, University of Glasgow, University Avenue, Glasgow, G12 8QQ, UK

[c]Laboratoire Léon Brillouin, CEA-CNRS, CE-Saclay, 91191 Gif-sur-Yvette, France

†Current address: Department of Chemistry and Materials Innovation Factory, University of Liverpool, 51 Oxford Street, Liverpool L7 3NY, UK

Contents

1. Materials and physical measurements

All experiments were carried under aerobic conditions using materials and solvents as received without any further purification. Elemental analyses (C, H, N) were performed by the University of Glasgow microanalysis service. Variable-temperature, solid-state direct current (dc) magnetic susceptibility data and AC magnetic susceptibility data were collected on a Quantum Design MPMS3 SQUID magnetometer at the University of Glasgow. Microcrystalline samples were prepared using a mortar and pestle in open air and then added to gelatin capsules with eicosane. Diamagnetic corrections were applied to the observed paramagnetic susceptibilities using Pascal's constants. The diamagnetic contribution of the sample holder and eicosane were corrected by measurements. Powder XRD measurements were collected on freshly prepared samples of $[Ho(H_2O)_5(HMPA)_2]I_3 \cdot 2HMPA$ (**2**) on a PANalytical X'Pert Pro MPD diffractometer (λ ($CuK\alpha_1$) = 1.5405 Å) on a mounted bracket sample stage, at the University of Glasgow. Single Crystal X-Ray diffraction data were collected using a Bruker D8 VENTURE diffractometer equipped with a Photon II CPAD detector, with an Oxford Cryosystems N-Helix device mounted on an IμS 3.0 (dual Cu and Mo) microfocus sealed tube generator at the University of Glasgow. Polarized neutron diffraction (PND) was measured on both $[Dy(H_2O)_5(HMPA)_2]I_3 \cdot 2HMPA$ (**1**) and **2** with the following procedure: a mm-sized single crystal was glued onto an aluminium pin, and the pin was mounted in a two-rotation-cradle on the end of a cold stick and inserted into a cryomagnet. Data for **1** (**2**) was collected for 3 (4) orientations of the crystal with respect to the magnetic field. The magnetic field in this setup is collinear with the vertical axis of the diffractometer. Experimental conditions were 5 K and 1 T and the experiment was performed on the 6T2 diffractometer operated by the Laboratorie Léon Brillouin on the Orphée reactor.

2. Crystallographic details

The structure of **2** was solved using ShelXT[1] and refined using ShelXL[2] within the program Olex2.[3] Positional parameters and anisotropic atomic displacement parameters (adps) were refined for all non-Hydrogen atoms, some of the atoms of the HMPA (Hexamethylphophoramide) were modelled over two partially occupied positions (0.7:0.3 for the coordinated HMPA and 0.5:0.5 for the free HMPA) as part of a disorder model, where isotropic adps were retained. Suitable distance and adp similarity restraints were applied to these atoms. Hydrogen atoms were placed in calculated positions and included as part of a riding model. The full details are available in the CIF (CCDC 2057601).

Table S1. Crystallographic data for complex **2**.

	2
Formula	$C_{12}H_{46}HoN_6O_7P_2{\cdot}3(I){\cdot}2(C_6H_{18}N_3OP)$
M_W/gmol^{-1}	1352.52
Crystal System	Monoclinic
Space group	*Cc*
a/Å	14.2486 (10)
b/Å	19.1836 (14)
c/Å	21.6652 (18)
α/°	90
β/°	106.281 (2)
γ/°	90
V/Å^3	5684.5 (7)
Z	4
T/K	150
λ/Å	0.71073
θ range for data collection/ °	3.0–25.0
D_c/g cm^{-3}	1.580
μ(Mo-K$_\alpha$)/ mm^{-1}	3.18
Meas./indep.(R_{int}) refl.	49581/9602 (0.039)
Obs. refl. [$I>2\sigma(I)$]	8975
$wR(F^2)$	0.0903
$R[F^2 > 2s(F^2)]$	0.0349
S	1.04
$\Delta\rho_{max,min}$/ eÅ^{-3}	1.037, -0.582

Table S2. Selected bond distances and angles for complex **2** (Å, º).

Ho1—O1	2.203 (6)	Ho1—O3W	2.329 (7)
Ho1—O2	2.204 (8)	Ho1—O4W	2.323 (7)
Ho1—O1W	2.349 (8)	Ho1—O5W	2.343 (7)
Ho1—O2W	2.321 (7)		
O1—Ho1—O2	179.6 (4)	O2—Ho1—O5W	90.9 (4)
O1—Ho1—O1W	90.4 (3)	O2W—Ho1—O1W	72.4 (3)
O1—Ho1—O2W	89.8 (3)	O2W—Ho1—O3W	71.6 (3)
O1—Ho1—O3W	89.3 (3)	O2W—Ho1—O4W	142.1 (3)
O1—Ho1—O4W	91.2 (3)	O2W—Ho1—O5W	144.9 (3)
O1—Ho1—O5W	88.9 (3)	O3W—Ho1—O1W	144.0 (3)
O2—Ho1—O1W	89.9 (4)	O3W—Ho1—O5W	143.4 (3)
O2—Ho1—O2W	90.6 (4)	O4W—Ho1—O1W	145.4 (3)
O2—Ho1—O3W	90.6 (4)	O4W—Ho1—O3W	70.5 (3)
O2—Ho1—O4W	88.4 (4)	O4W—Ho1—O5W	73.0 (3)
		O5W—Ho1—O1W	72.6 (3)

Table S3. Shape analysis for complexes **1** and **2**. The lowest CShMs value, is highlighted. Continuous shape measures analysis estimates the distortion from the perfect polyhedron, where 0 corresponds to the ideal structure.[4-6]

	Ho	**Symmetry**	**Ideal polyhedron**
HP-7	34.403	D_{7h}	Heptagon
HPY-7	25.787	C_{6v}	Hexagonal pyramid
PBPY-7	**0.090**	$\boldsymbol{D_{5h}}$	**Pentagonal bipyramid**
COC-7	8.109	C_{3v}	Capped octahedron
CTPR-7	6.246	C_{2v}	Capped trigonal prism
JPBPY-7	2.751	D_{5h}	Johnson pentagonal bipyramid J13
JETPY-7	24.569	C_{3v}	Johnson elongated triangular pyramid J7

	Dy	**Symmetry**	**Ideal polyhedron**
HP-7	34.315	D_{7h}	Heptagon
HPY-7	25.127	C_{6v}	Hexagonal pyramid
PBPY-7	**0.131**	$\boldsymbol{D_{5h}}$	**Pentagonal bipyramid**
COC-7	7.780	C_{3v}	Capped octahedron

CTPR-7	5.911	C_{2v}	Capped trigonal prism
JPBPY-7	2.617	D_{5h}	Johnson pentagonal bipyramid J13
JETPY-7	24.592	C_{3v}	Johnson elongated triangular pyramid J7

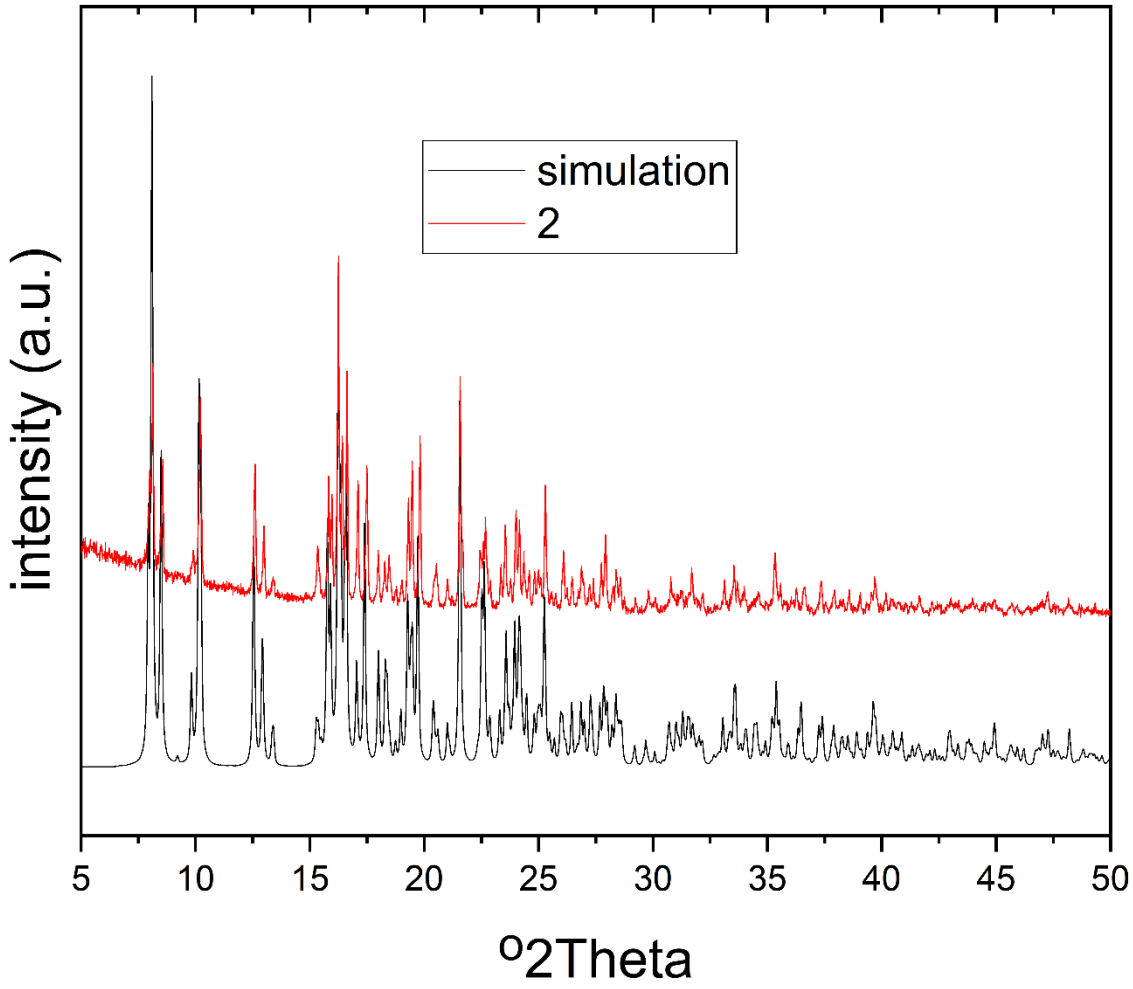

Fig. S1 The powder X-ray diffraction pattern of **2**. The black line represents the simulated powder X-ray diffraction pattern generated from single-crystal data collected at 150 K, and the red line represents the experimental data measured at ambient temperature.

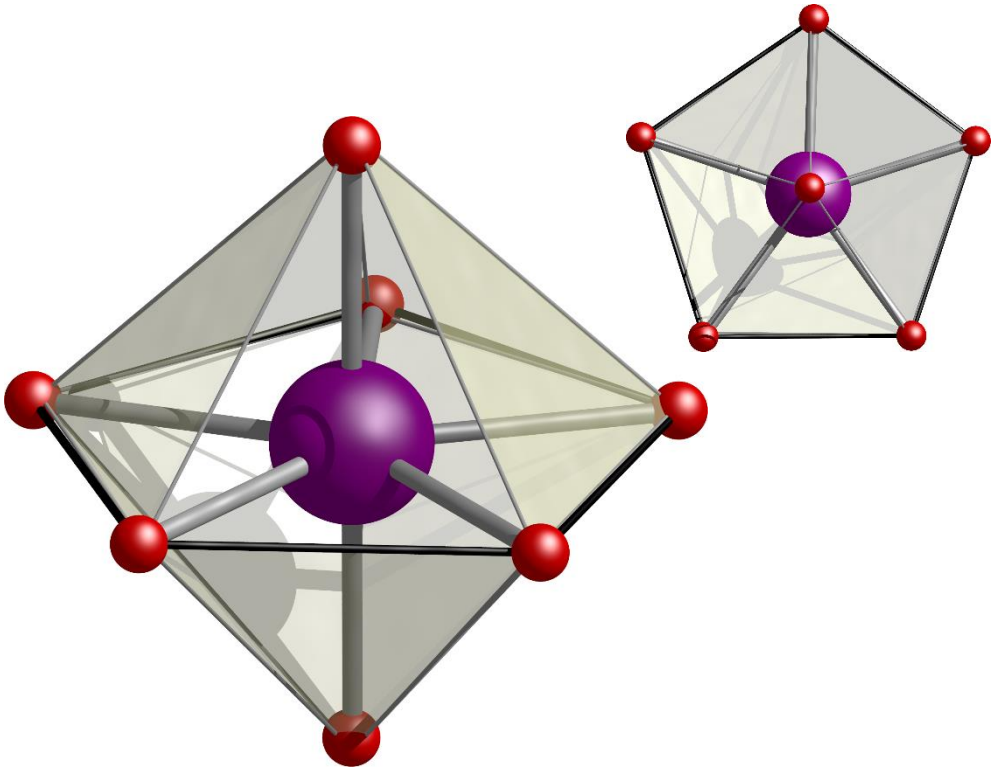

Fig. S2 Comparison of the calculated (with SHAPE)[4-6] and experimental compressed pentagonal bipyramidal coordination sphere for the Ho(III) ion in **2**. (Inset) The highlighted pentagonal bipyramidal plane. Ho, magenta; O, red.

3. **Magnetic Properties**

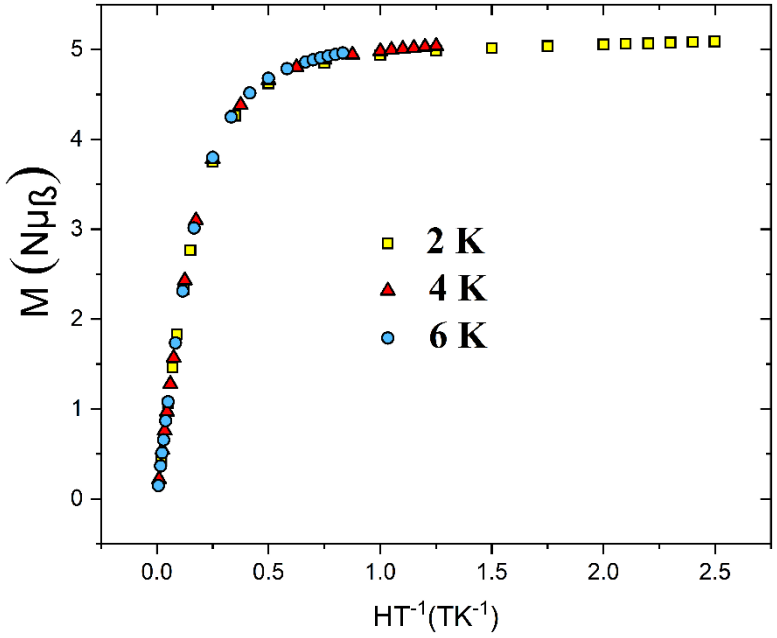

Figure S3. Reduced magnetization plot for **2** at 2 K, 4 K and 6 K.

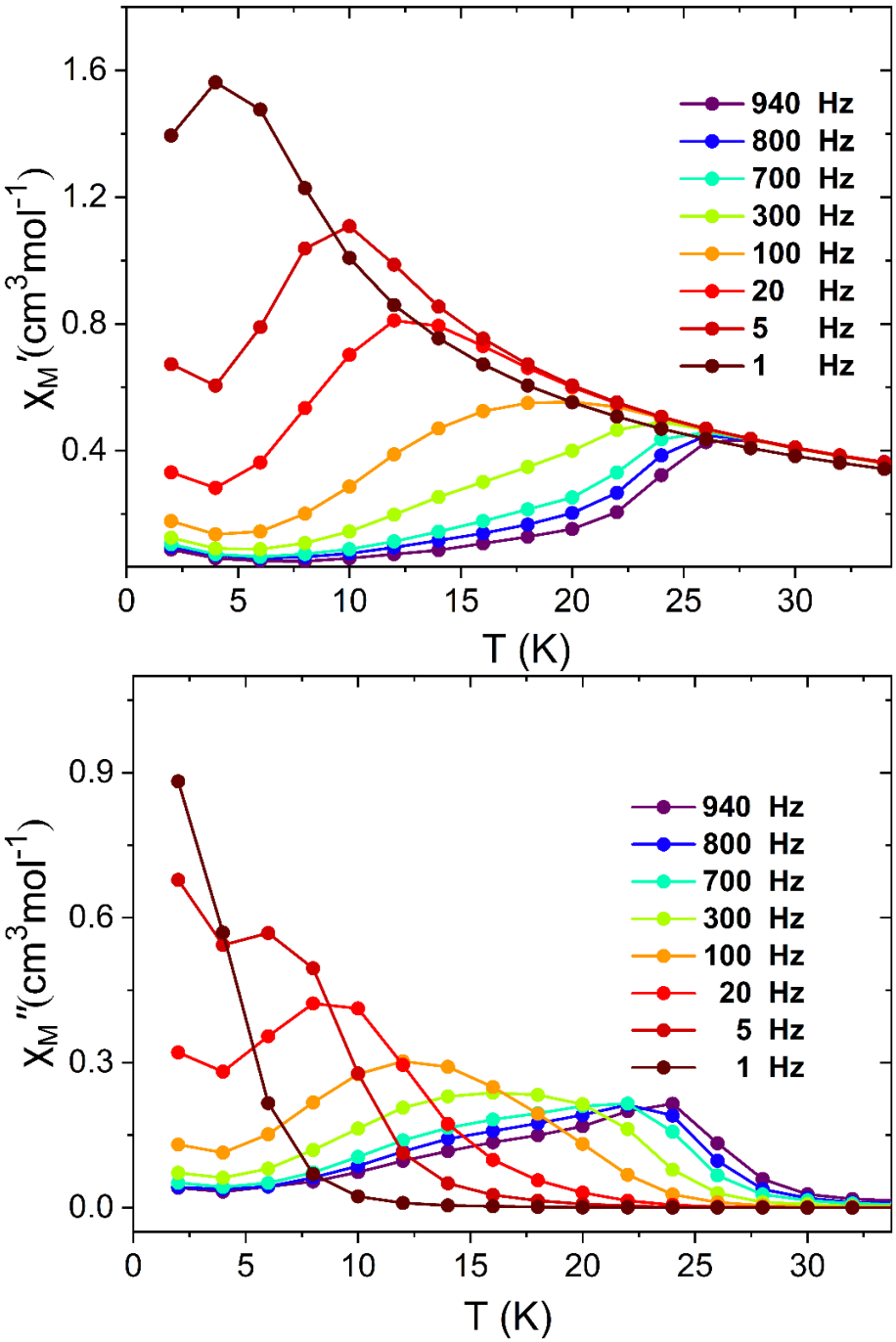

Fig. S4 Temperature dependence of the in-phase, χ'_M (upper) and out-of-phase, χ''_M (lower) ac susceptibility, in zero dc field, for **2** with ac frequencies of 1–940 Hz.

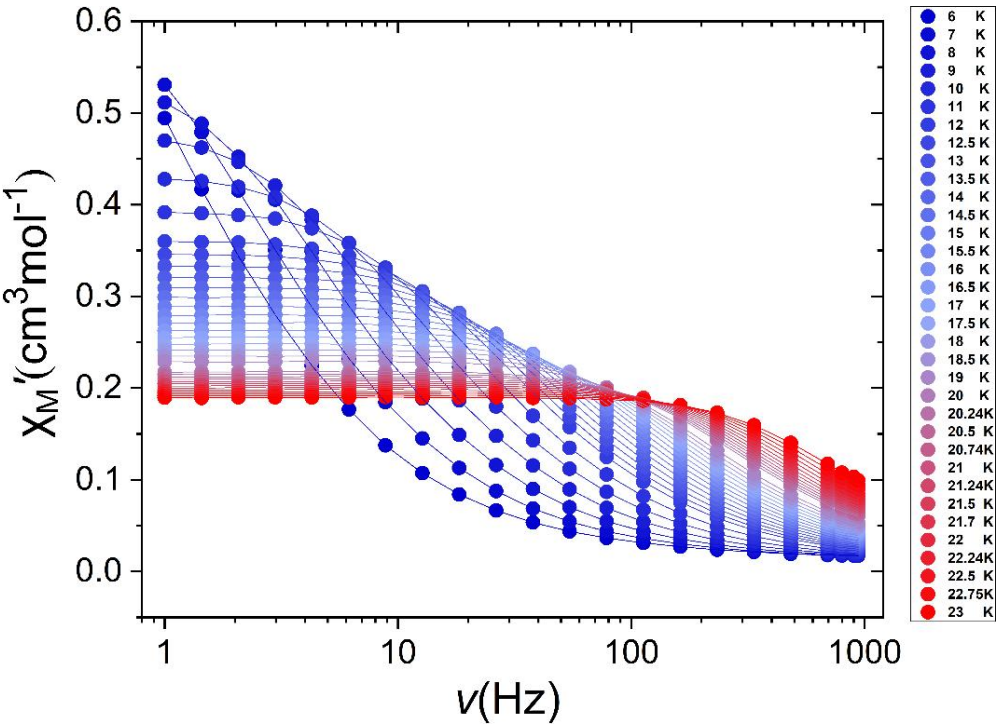

Fig. S5 Frequency dependence of the in-phase, χ'_M ac susceptibility, in zero dc field, for **2** with ac frequencies of 1–940 Hz. The solid lines correspond to the best fit to Debyes's law.[7]

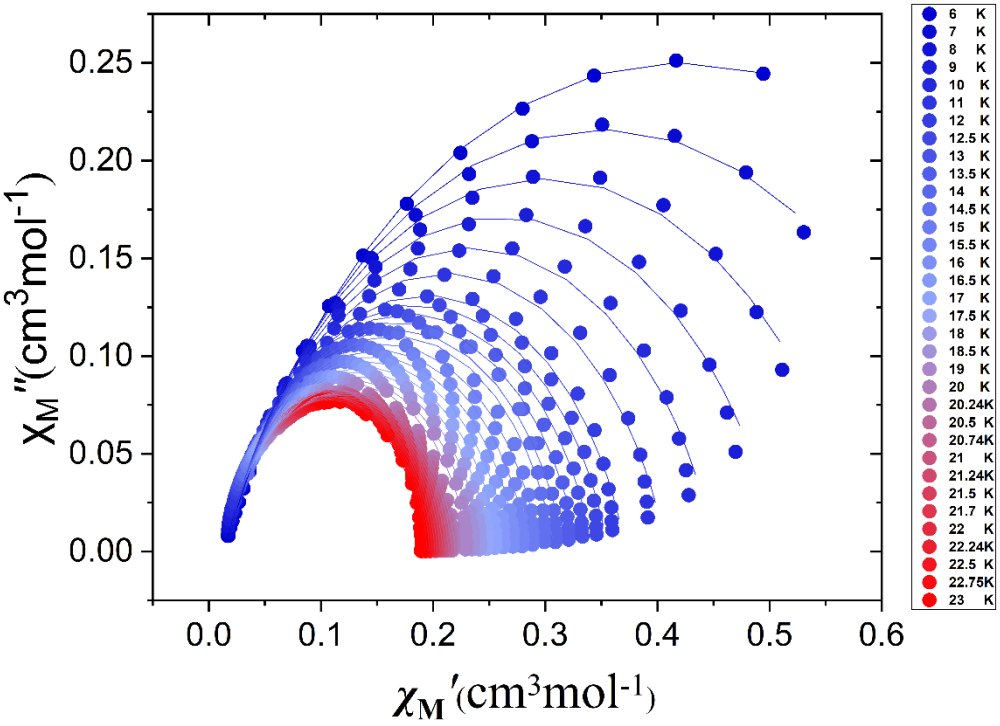

Fig. S6 χ''_M vs χ'_M plot of the AC magnetic susceptibility of **2** in zero dc field. The solid lines correspond to the best fit to Debye's law.[7]

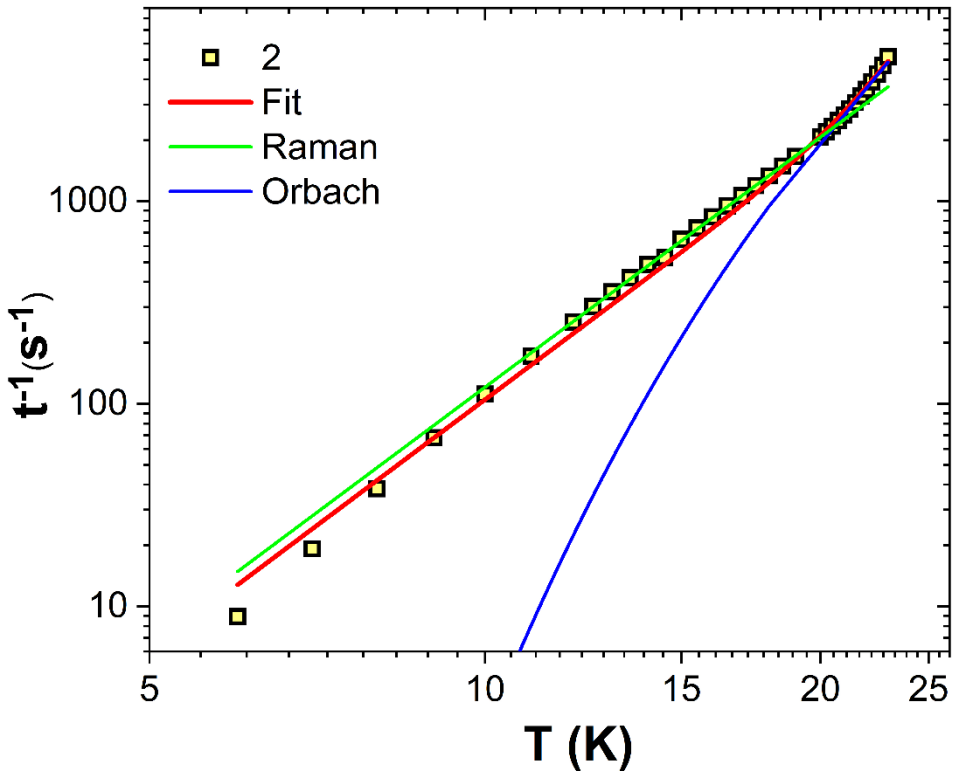

Fig. S7 Log-Log plot of the relaxation times, τ^{-1} versus T for **2**. The data were analysed using the equation: $\tau^{-1} = CT^n + \tau_0^{-1} \exp(-U_{eff}/T)$. The best fit (red line) gives n = 4.11, C = 8.0 10^{-3} K^{-n} s^{-1}, τ_0 = 4.77 x 10^{-9} s and U_{eff} = 270 K.

4. Ab initio calculations

Calculations on **2** were carried out as complete active space self-consistent field (CASSCF) calculations using the CASSCF/RASSI-SO/SINGLE_ANISO approach in OpenMolcas version 18.09 through the pymolcas interface.[8, 9] The structure determined from X-ray diffraction was used for the molecular geometry of the compound, including solvent atoms and counterions. For the disordered parts of the crystal structure, the groups with the largest occupancy were used in the calculations. The basis sets employed for the atoms in the structure were of the ANO-RCC family, using 8s7p5d3f2g1h (pVTZ) for Ho, 7s6p4d2f1g (pVTZ) for I, 3s2p1d (pVDZ) for O, 4s3p (VDZ) for P, 3s2p (VDZ) for N and C and 2s (VDZ) for H. The calculations were performed with 35 quintuplets arising from 10 f-electrons in Ho(III).

Table S4. CASSCF+RASSI-SO computed relative energies (in K) along with *g* tensors and deviations from the principal magnetisation axis for complex **2**.

Levels	E (K)	g_{zz}	Δ_{Tun} (cm^{-1})	Angle (°)	Composition of m_J levels[a]
1 2	0 2.320 x 10^{-3}	19.96	0.00161	-	49.9%|+8>+49.9|-8> 49.9%|-8>+49.9|+8>
3 4	259.88 261.17	19.25	0.896	86.72	14.7%|+3>+26.8%|+1>+26.8%|-1>+14.7%|-3> 23.8%|+2>+28.4%|0>+23.8%|-2>
5 6	316.36 317.42	14.01	0.743	86.59	10.1%|+3>+20.8%|+2>+10.2%|+1> +10.2%|-1>+20.8%|-2>+10.1%|-3> 15.5%|+3>+11.1%|+1>+11.1%|-1>+15.5%|-3>
7 8	335.21 339.40	11.58	2.912	81.84	11.5%|+3>+17.6%|+2>+25.6%|0> +17.6%|-2>+11.5%|-3> 13.9%|+7>+12.6%|+1>+12.6%|-1>+13.9%|-7>
9 10	348.52 350.51	13.16	1.386	0.88	39.6%|+7>+39.6%|-7> 32.0%|+7>+32.0%|-7>
11 12	381.27 387.20	12.57	4.118	80.26	24.8%|+4>+12.8%|+3>+12.8%|-3>+24.8%|-4> 14.2%|+4>+16.3%|+3>+10.8%|0> +16.3%|-3>+14.2%|-4>
13 14	410.52 421.23	9.99	7.447	72.90	25.3%|+4>+13.3%|+2>+13.3%|-2>+25.3%|-4> 10.7%|+6>+32.4%|+5>+32.4%|-5>+10.7%|-6>
15 16	425.90 453.41	4.94	19.12	75.46	17.2%|+6>+20.6%|+5>+20.6%|-5>+17.2%|-6> 29.5%|+6>+15.0%|+5>+15.0%|-5>+29.5%|-6>
17	457.01	-	-	-	33.8%|+6>+33.8%|-6>

a Only >10% contributions are given.

Table S5. The *ab initio* computed crystal field parameters for complex **2**.

k	q	K^2	B_k^q
2	-2	1.50	-0.15131997725169E+00
2	-1	6.00	0.13868748188887E+00
2	0	1.00	-0.69713815284121E+00
2	1	6.00	-0.28220855227846E+00
2	2	1.50	0.38359810855775E+00
4	-4	17.50	0.57504622753594E-03
4	-3	140.00	0.73662060889561E-03
4	-2	10.00	0.65719677867509E-03
4	-1	20.00	-0.28042202397960E-02
4	0	1.00	-0.51775543823050E-02
4	1	20.00	-0.48683823119794E-03
4	2	10.00	-0.12720539495416E-02
4	3	140.00	0.93854550916413E-02
4	4	17.50	0.36792799472121E-03
6	-6	57.75	-0.12933535744858E-03
6	-5	693.00	0.10919224997567E-03
6	-4	31.50	-0.75958867381512E-05
6	-3	105.00	0.10577426427578E-04
6	-2	26.25	0.98313670421568E-06
6	-1	42.00	0.32277851144246E-04
6	0	1.00	-0.18403994617629E-04
6	1	42.00	0.26643800551109E-04
6	2	26.25	0.36131535386007E-04
6	3	105.00	-0.86624208898695E-04
6	4	31.50	0.46032804008210E-05
6	5	693.00	0.32483843350770E-05
6	6	57.75	0.32383304802819E-05

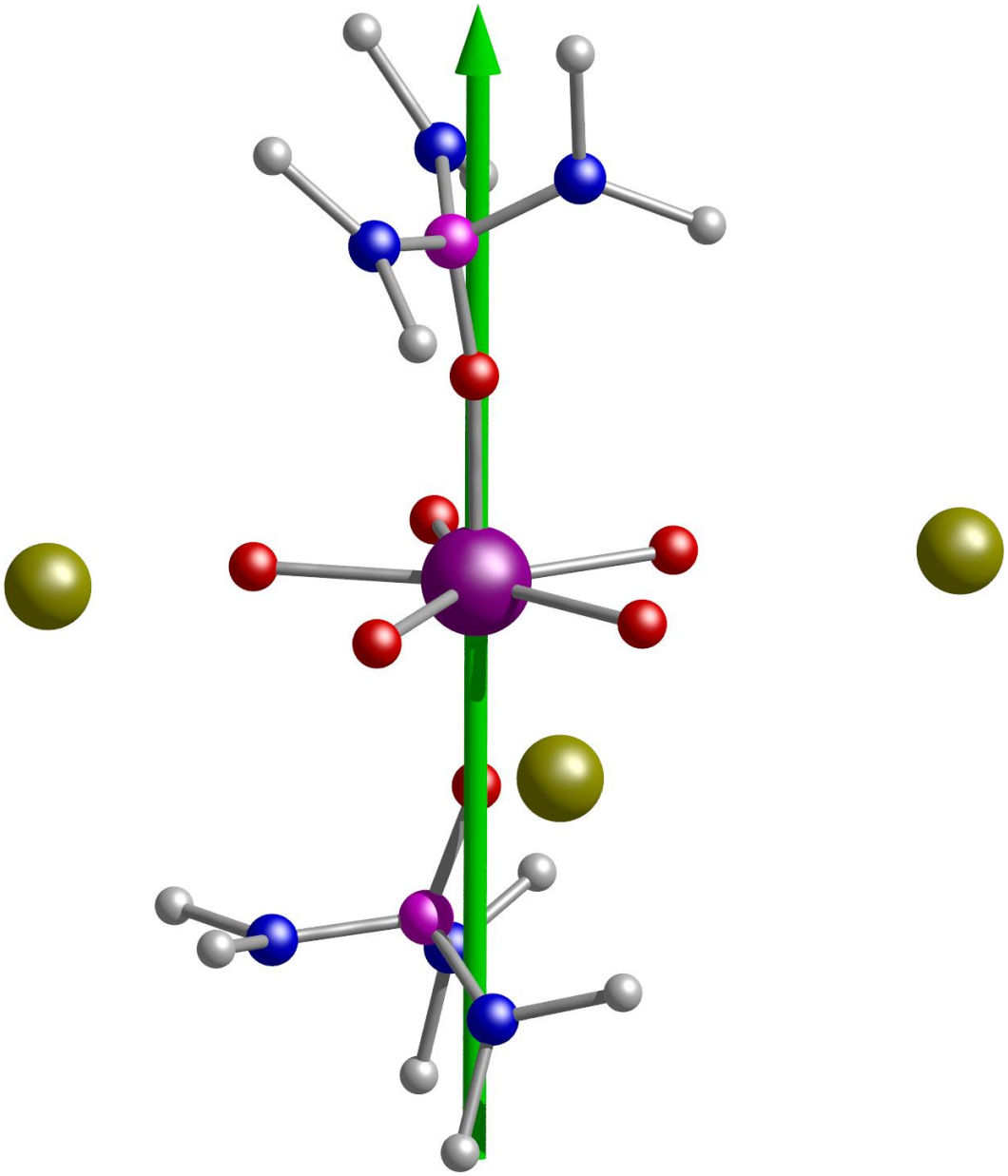

Fig. S8 *Ab initio* computed g_{zz} orientation of the ground pseudo doublets for complex **2**. Colour code: Ho, magenta; O, red; N, blue; P, pink; C, gray; I, dark yellow. Hydrogens atoms, co-crystalized HMPA molecules and disorder components are omitted for clarity.

5. Using X-ray structures for refinement against polarized neutron diffraction data

For this study, we did not have access to unpolarized neutron diffraction data to refine the nuclear structures for **1** or **2**. To investigate the credibility of instead using an structure refined from x-ray diffraction when refining site susceptibilities with PND data, we studied the effect of exchanging the structural model used to refine a site susceptibility tensor against the same PND data. It is well established that X-ray crystal structures lead to artificially short bond X-H bond lengths, because electron density is shifted from near the nucleus of the hydrogen atom into the covalent bond. Therefore, three different ways of obtaining the structural model were studied: X-ray structure with as-refined bond lengths to hydrogen (X_{short}), X-ray structure with bond lengths to H equal to those obtained from neutron diffraction refinement (X_{long}), conventional neutron diffraction structure refinement (ND). The study was undertaken for two different molecules, $Dy(dbm)_3bpy$ (dbm=1,3-diphenyl-1,3-propanedione) (**3**) and $CoBr_2(tmtu)_2$ (tmtu=1,1,3,3-tetramethylthiourea) (**4**). For **3**, both the nuclear structure along with the refinement of the PND-data and the X-ray structure have earlier been reported,[10, 11] and for **4** the X-ray structure had also been published.[12] The complete refinement of the nuclear structure of **4** and the execution of the PND experiment will be reported elsewhere.[13] Here, the focus is on the effect of exchanging the structural model in the PND refinement.

The results for **3** in terms of tensor elements (χ_{ij}) are shown in Table S6 along with the total value of χ^2 for six orientations of the magnetic field with respect to the crystal of the compound that was being measured. In addition, we show the angular discrepancy between the easy-axis direction for the neutron diffraction refinement and the other two models. A final comparison was made between the three tensors, based on a similarity index originally developed for anisotropic displacement tensors, but used here for the magnetic susceptibility tensors.[14] The index, S_{12}, rates the percentage difference between two second rank tensors, such that a value of 0 is obtained for fully identical tensors.

Table S6. Tensor elements (χ_{ij}) in the basis of the Cambridge Crystallographic Subroutine Library,[15] total χ^2-value, easy-axis discrepancy compared to the ND-direction, and similarity index, S_{12}, for the refinement of PND-data for **3** against three different structural models for simulation of nuclear structure factors. Unit on χ_{ij}'s is $\mu_B\, T^{-1}$.

	χ_{11}	χ_{22}	χ_{33}	χ_{23}	χ_{31}	χ_{12}	χ^2	EA (°)	S_{12}
ND	0.69	7.99	3.29	-4.86	1.21	-1.87	3.67	0	0
X_{long}	0.63	8.03	3.29	-4.88	1.25	-1.90	3.86	0.11	1.32
X_{short}	0.61	7.72	3.12	-4.66	1-09	-1.75	4.16	0.52	0.37

For **4**, in addition to probing the two different between X-ray models (X_{short} and X_{long}), we used two different approaches to refining H-atom positions from the X-ray diffraction data in SHELXL.[2] In one approach, the H-positions were refined with the "AFIX 137"-keyword that restricts a CH_3-group to have tetrahedral angles but allows it to rotate freely around the fourth bond to C. In the other approach, "AFIX 33" was used, which keeps an ideal tetrahedral geometry, but fixes the rotation angle such that the CH_3-group becomes staggered. The results for four of the models are shown in Table S7. For X_{long} with the "AFIX 33"-keyword a successful refinement against the diffraction data could not be completed. The refinement was performed against four directions of applied magnetic field with respect to the molecule in the same beamline setup as that described in the main text.

Table S7. Tensor elements (χ_{ij}) in the basis of the Cambridge Crystallographic Subroutine Library,[15] total χ^2-value, easy-axis discrepancy compared to the ND-direction, and similarity index, S_{12}, for the refinement of PND-data for **4** against four different structural models for simulation of nuclear structure factors. Unit on χ_{ij}'s is $\mu_B\, T^{-1}$.

	χ_{11}	χ_{22}	χ_{33}	χ_{23}	χ_{31}	χ_{12}	χ^2	EA (°)	S_{12}
ND	0.23	0.99	1.40	-0.97	-0.47	0.25	2.83	0	0
X_{long}(137)	0.21	0.96	1.37	-1.00	-0.44	0.32	5.24	0.72	3.9
X_{short}(33)	0.54	0.79	1.43	-0.59	-0.73	0.17	23.75	15	11.3
X_{short}(137)	0.30	0.92	1.36	-0.96	-0.51	0.35	5.32	3.0	5.2

In the results of **3**, we see that the susceptibility tensors obtained with an X-ray structure are very similar to the tensor obtained based on a nuclear structure. The X_{long}-model for **3**, gives a slightly better χ^2-value and a smaller angular discrepancy, while the X_{short}-model gives a smaller, and thus

better, similarity index. Overall, the difference between the models is negligible, and on the order of the uncertainty of the model. For **4**, the agreement parameters for $X_{short}(33)$ show that this model is unviable for the description of the magnetic susceptibility tensor of **4**. For the two other approaches based on X-ray diffraction, there is no clear distinction between the models. $X_{long}(137)$ gives slightly better agreement with the ND-model, based both χ^2, easy axis angle and similarity index, but similar to the results for **3**, the difference between the models is estimated to be on the order of the model uncertainty. These results show that it *is* viable to use an X-ray structure to refine susceptibility tensors based on PND and that the elongation of bonds to H-atoms may provide an improvement to the modelling of PND-data.

With these results in mind, for this study we used structures with elongated bonds to H-atoms. The only bonds to H that are in the structures of **1** and **2** are the C-H-bonds in the CH_3-groups of the HMPA-ligands and the O-H-bonds in the equatorial water molecules. A survey of known molecules in the CSD found that from neutron diffraction studies the C-H-bonds have mean lengths of 1.077(29) Å[16]. The bond lengths in the methyl groups of **1** and **2** were set to these values, and CH_3-groups were refined using "AFIX 137". The bond lengths between O and H in the equatorial water molecules were not changed, but kept at the values obtained from a refinement using DFIX restraint of 0.85 Å with an esd of 0.02 Å. In the structure solution of **2**, the bond lengths in the equatorial water molecules had already been fixed to successfully refine the structure, and in both structures, the hydrogen positions in the equatorial water molecules are not only influenced by the bonding to O, but also by the interaction with I^--counterions and the solvent HMPA-ligands. Therefore, these bond lengths were left as refined. The change in R-values for **1** and **2** on going from the as-refined bond lengths (H_{short}) to the elongated bond lengths (H_{long}) are small and presented in Table S8.

Table S8. R-values of the refinement against X-ray diffraction data with short (H_{short}) and elongated (H_{long}) bonds to H-atoms for **1** and **2**.

R-values [%] (R1, wR2)	**1**	**2**
H_{short}	2.41, 5.35	3.58, 9.43
H_{long}	2.44, 5.42	3.58, 9.48

We note also that the use of an X-ray structure determination for refinement against PND-data has earlier been reported.[17]

6. PND data reduction and refinement details

The data collection on **1** and **2** was performed as described in the main text. To keep the crystal orientation fixed with respect to the external magnetic field, the only rotation that is performed of the crystal with respect to the incoming neutron beam is a rotation of the φ-axis of the diffractometer, that is the vertical direction in the laboratory frame. The data collections are summarized in Table S9.

Regions of interest (ROIs) containing potential peaks were extracted from the raw images using a suite of in-house data reduction programs from the LLB. Based on these ROIs, the crystal orientations were refined by fitting an orientation matrix with the 100 K structure of **1** and the 150 K structure of **2**. Only ROIs, for which the deviation of either h, k, or l was less than 0.2 from the closest integer value, were kept and used to calculate flipping ratios for the further analysis. The flipping ratios obtained in this way are plotted as a function of 2θ in Figure S9 and Figure S10 for **1** and **2** respectively.

Table S9. Summary of data collections and the reduced data from **1** and **2**. Numbers in parentheses constitute a second setting of the detector. Notice that for **1**, the first orientation was measured by making slices of reciprocal space around expected peak positions, and therefore, the minimum, maximum and incremental values of phi for a single rotation are not applicable here and therefore not noted in the table.

1				
	O1	O2	O3	O4
Detector position, gamma [degrees]	N/A	17.0	17.0	N/A
Phi min, max, increment [degrees]	N/A	43.8, 350.0, 0.1	10.0, 284.4, 0.1	N/A
No. of ROIs	74	149	54	N/A
Orientation refinement $\chi^2, \%$	3.64	6.11	2.03	N/A
Peaks kept after orientation refinement	71	127	53	N/A
2				
	O1	O2	O3	O4
Detector position, gamma [degrees]	17	17	17	17 (40)
Phi min, max, increment [degrees]	10.0, 350.0, 0.1	10.0, 336.9, 0.1	10.0, 304.0, 0.1	10.0, 350.0, 0.1 (10.0, 44.6, 0.1)
No. of ROIs	82	120	11	30
Orientation refinement χ^2 [%]	9.72	11.14	5.13	11.86
Peaks kept after orientation refinement	31	33	6	7

Peaks kept after |FR-1|>2σ	31	29	6 (not subject to requirement)	7 (not subject to requirement)

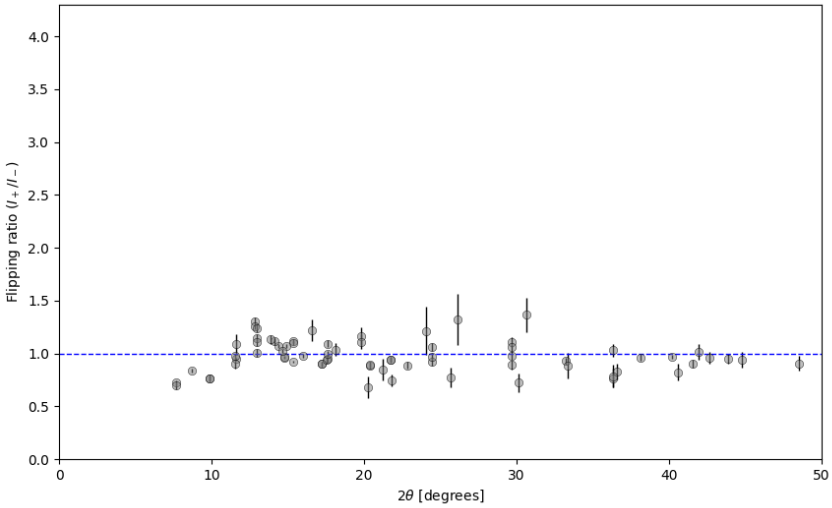

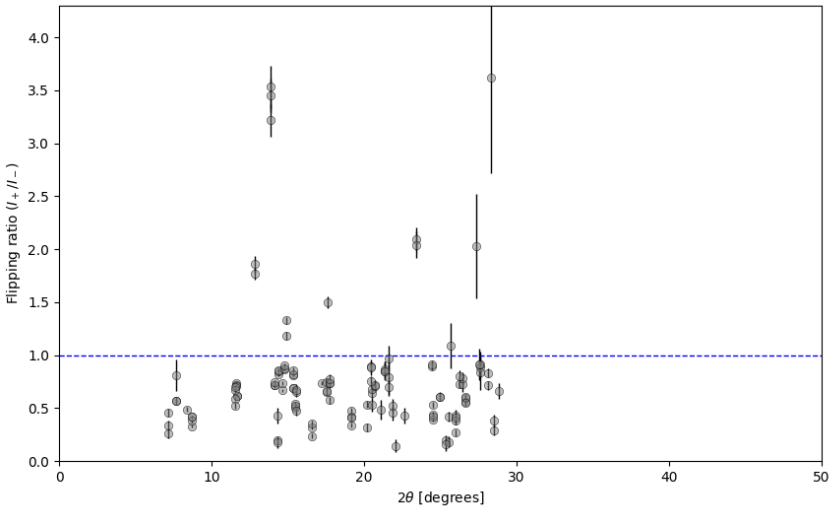

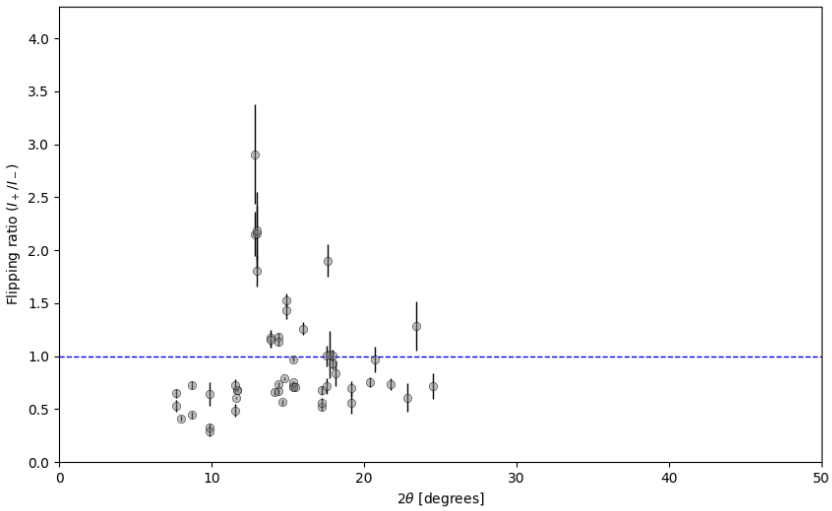

Figure S9. Flipping ratios for **1** plotted as a function of scattering angle, 2θ, for orientations 1, 2 and 3 respectively. The blue line at a flipping ratio of 1 indicates the expected value in the absence of a magnetic structure.

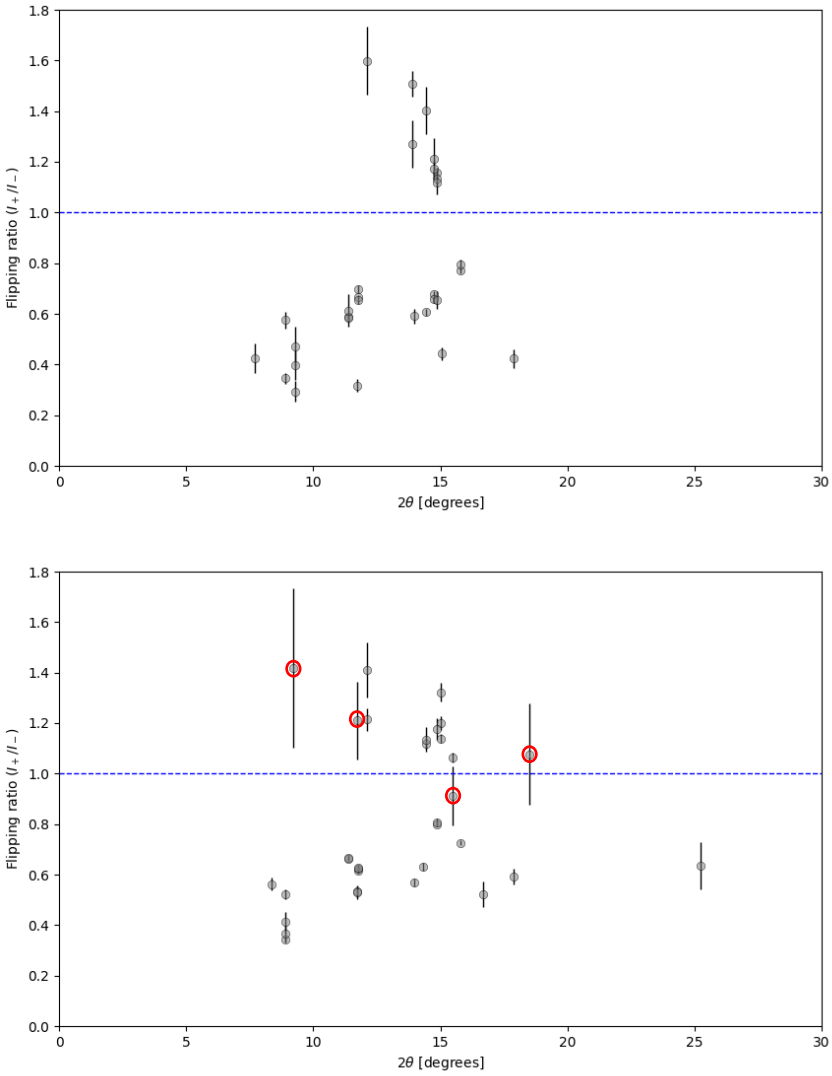

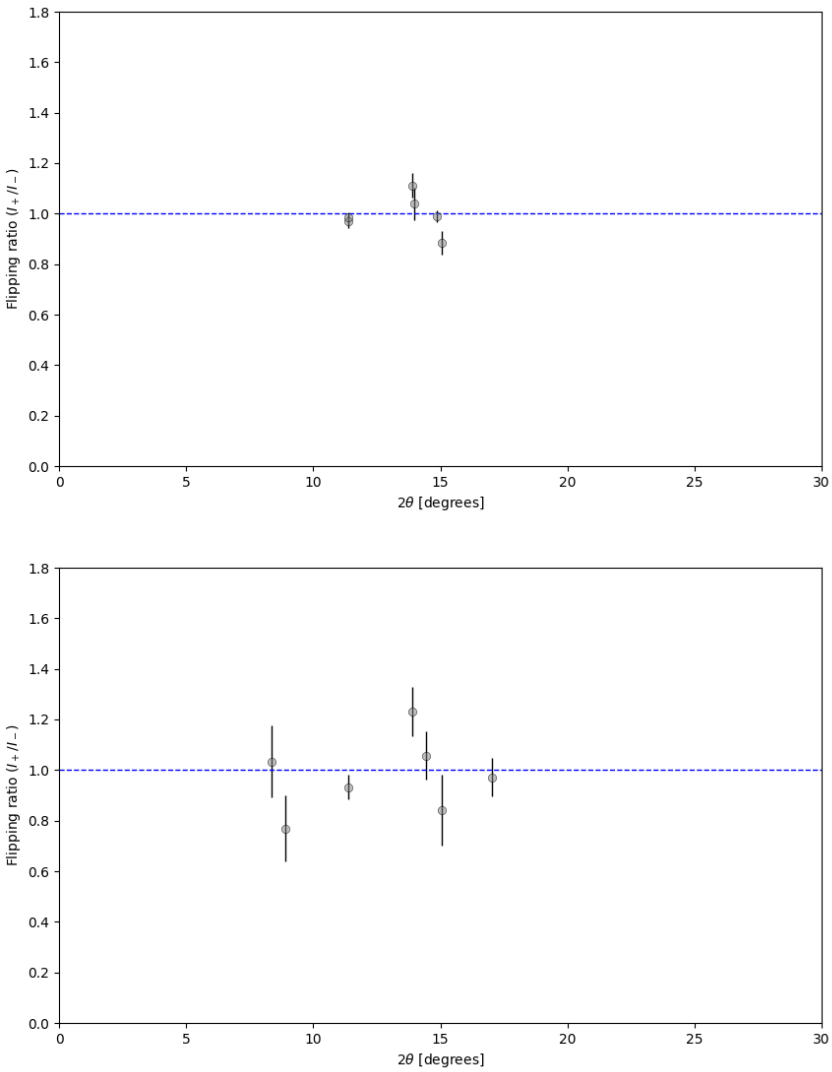

Figure S10. Flipping ratios for **2** plotted as a function of scattering angle, 2θ for orientations 1, 2, 3 and 4 respectively. The blue line at a flipping ratio of 1 indicates the expected value in the absence of a magnetic structure. The flipping ratios marked with a red circle for orientation 2 were omitted for some of the models attempted for **2**.

An important success criterium of the PND experiment is the directions of the magnetic field with respect to the crystal. Preferably, these directions should be different enough to probe different directions of the molecular magnetization, for the refined parameters to be uncorrelated. To judge whether this has been achieved, we have mapped the magnetic field directions based on the orientation matrices for each orientation onto the molecule in the asymmetric unit of the crystal structure in Figure S11. As seen in Figure S11, a large spread in the field directions was successfully achieved for **1**. For **2**, we observe that one set of field directions were in the horizontal plane (blue, orange), while the other two field directions were both along the axial direction and transverse directions (red, green) of the symmetry related molecules in the unit cell (Figure S12).

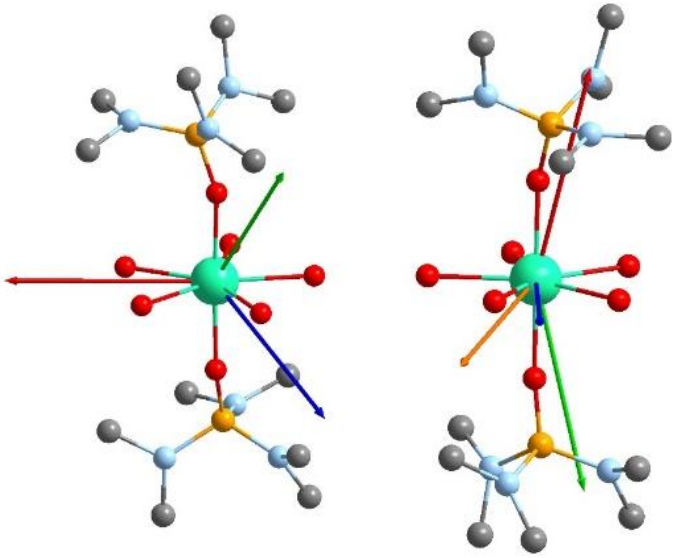

Figure S11. Molecular structures of **1** (left) and **2** (right) shown as ball-and-stick models and with hydrogen atoms omitted. Magnetic field for orientations 1, 2, 3 and 4 are shown as red, green, blue, and orange arrows, respectively. Ln: teal, O: red, P: orange, N: blue, C: grey.

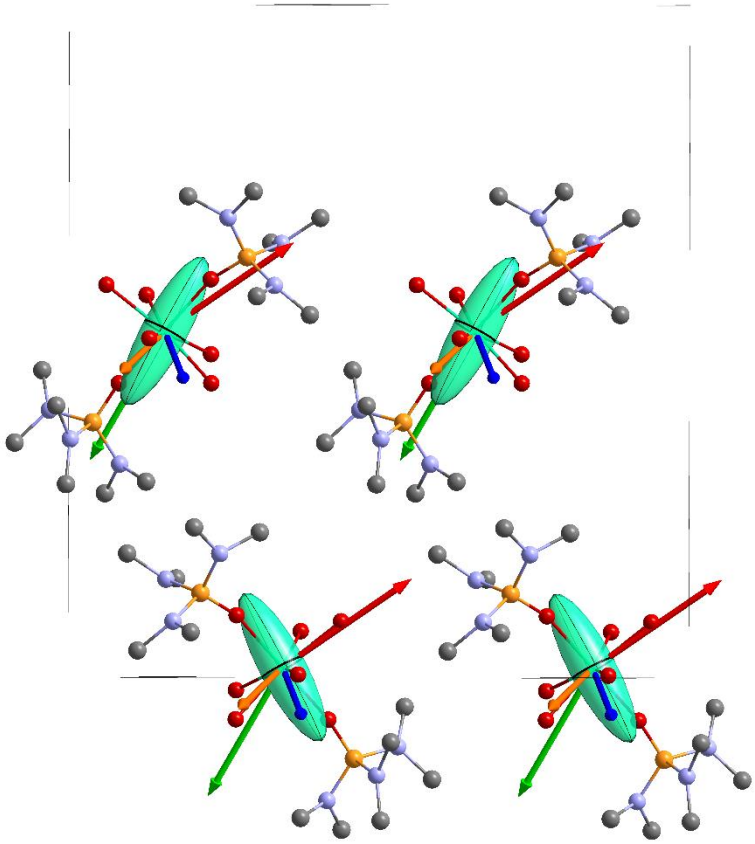

Figure S12. Unit cell of **2** with all 4 symmetry-related molecules and their relation to the magnetic field directions of the 4 crystal orientations described in the text. Hydrogen atoms, HMPA co-crystallized molecules and counterions have been omitted. Roughly speaking, the magnetic fields of orientation 1 and 2 (red and green) are probing both the axial and transverse elements of the

magnetic susceptibility tensor, whereas orientation 3 and 4 are exclusively probing transverse elements.

Given the likeness of orientations 1 and 2 and of orientations 3 and 4, effectively the (red,green)-orientations are probing both the axial and transverse elements, whereas the (blue,orange)-orientations are only probing transverse elements of the magnetic susceptibility tensor for **2**.

The refinement of the atomic site susceptibility tensor for **1** is straightforward, due to the well-separated field orientations, the overall number of flipping ratios, and their relatively small standard deviations. The final model is shown in the main text, and the agreement between the data and the final model is shown in Figure S13 and Table S10.

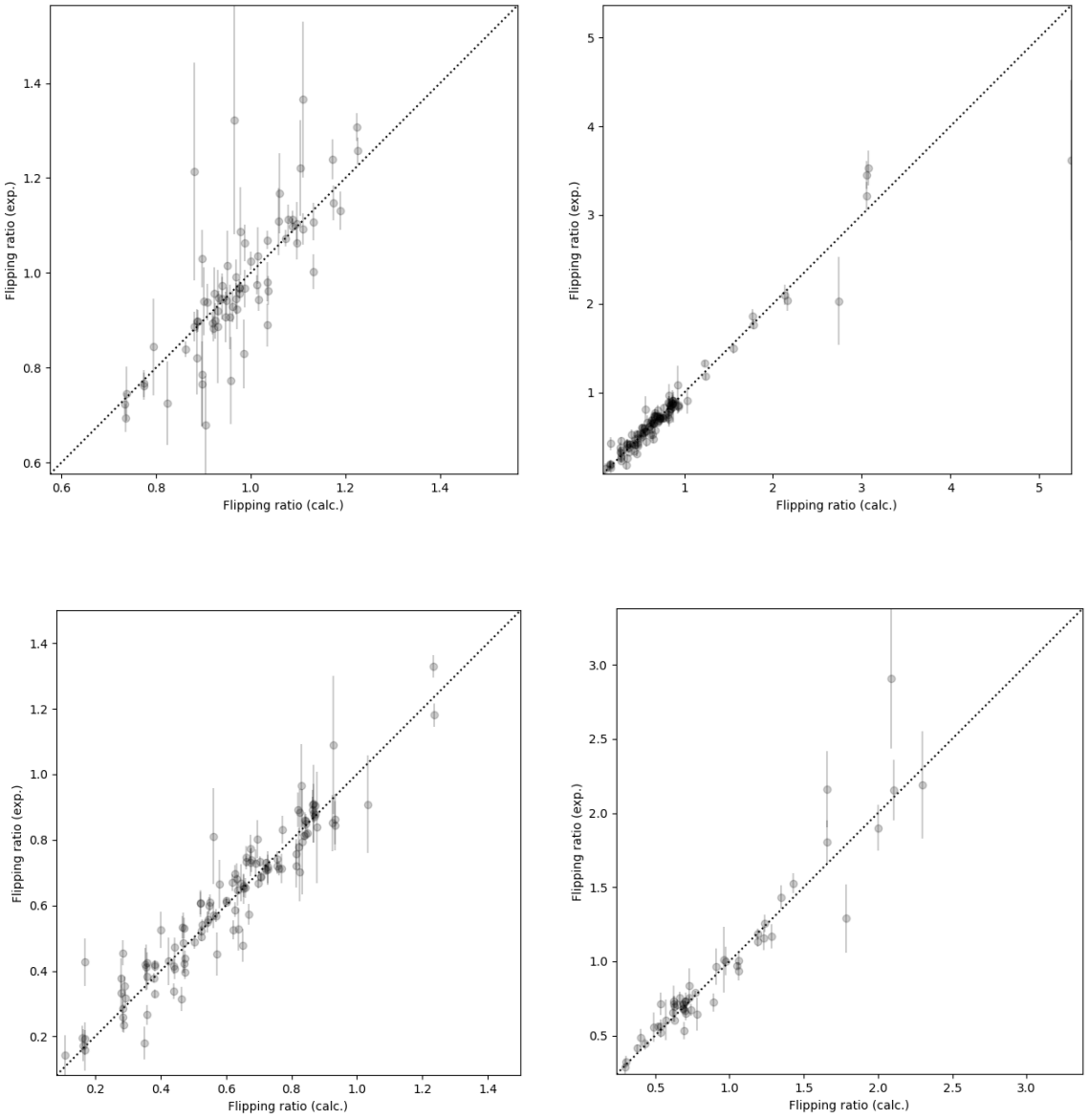

Figure S13. Agreement between model and data for **1**. The plots show the calculated and experimental flipping ratios for orientation 1, orientation 2, a zoom of orientation 2 and orientation 3 from top left to bottom right respectively.

Table S10. Agreement between model and data for 1 represented by χ^2-values based on the flipping ratios.

	O1	O2	O3	Overall
1	1.81	3.04	2.08	2.49

For **2** on the other hand, due to the scarcity of well-determined data, we approach the fit to these data with more caution. The two orientations for **2** with a "equatorial" magnetic field (3 and 4) contain very few flipping ratios, but we notice that the flipping ratios are all close to 1, and that the flipping ratios for the orientations with the magnetic field in an "axial" direction to a larger extent show a deviation from 1. This follows the expected pattern, assuming that the primary anisotropy axis is along the O-Ln-O-direction, because magnetic fields that are perpendicular to the easy axis direction in an anisotropic compound will only induce small magnetic moments, giving rise to small deviations of the flipping ratio from 1. We note that a similar pattern is observed for **1**, where the first orientation is almost perfectly aligned with the horizontal direction within the molecule, and the flipping ratios here are also very close to 1. These flipping ratios are all important in the refinement of the atomic susceptibility tensors, as the measurements that show the near absence of a magnetic moment, when the magnetic field is applied along these directions impose restraints on the maximum values of the atomic susceptibility tensor of **2**.

As an exemplification of this happening, we attempt a refinement of the susceptibility tensor for **2** in the case where orientation 3 and 4 have been omitted from the refinement (**model 1**). In this model, the main anisotropy axis is oriented towards the horizontal plane within the molecule. Furthermore, the eigenvalues, that are in this case unbounded by the flipping ratios close to 1 in the transverse plane, increase dramatically, and the susceptibility tensor in that case refines to give eigenvalues of $47\ \mu_B\ T^{-1}$, $7\ \mu_B\ T^{-1}$ and $2\ \mu_B\ T^{-1}$. The agreement factors between this model and the data are shown in Table S11. They are not markedly different from the agreement factors for some of the other models that we have tried with this data (vide infra), but we note that the susceptibility value of $47\ \mu_B\ T^{-1}$ is unrealistically large for a single Ho(III) ion. The susceptibility tensor refined for this model is visualized on top of the molecular structure of **2** in Figure S14.

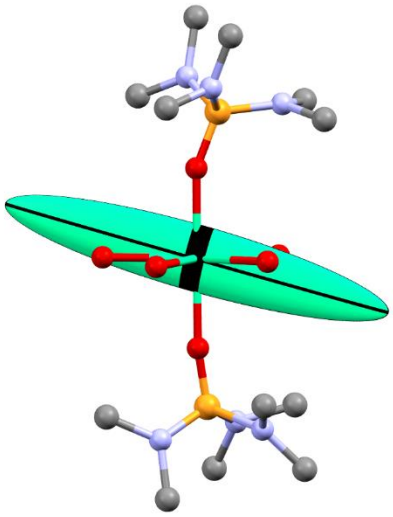

Figure S14. Atomic susceptibility tensor of **2** refined without orientation 3 and 4 to show the influence of refining an atomic susceptibility tensor without the influence of the transverse orientations.

With **model 1** showing that the orientations 3 and 4 are necessary for the refinement of the susceptibility tensor to give reasonable susceptibility values, we assert that the scarcity of data along these two directions make it imperative to use all available flipping ratios of those directions. For the second orientation measured on **2**, however, we have also tested a model where we removed those flipping ratios from orientation 1 and 2 that fulfil the relation |FR-1|<2σ (FR: Flipping Ratio; **model 2**). This is an analogous requirement to the requirement that data in a conventional diffraction experiment must be significantly different from the background, with the "background" in a flipping ratio experiment being 1. This requirement only filters out 4 flipping ratios from orientation 2 (marked with red in Figure S10), and no flipping ratios are filtered out from orientation 1 with this cut-off value. Exclusion of these 4 data points means that the refined experimental magnetic easy-axis of **2** has a deviation of roughly 23(1)˚ with the O-Ho-O-direction, compared to 25(1)˚ obtained by using all orientations and including the 4 data points in the refinement (**model 3**). The eigenvalues in the two models are $(10.1\ ,\ 2.6\ ,\ -1.8)\ \mu_B\ T^{-1}$ and $(10.7\ ,\ 3.0\ ,\ -2.5)\ \mu_B\ T^{-1}$ for model 2 and 3, respectively.

Having tested the effect of the omission of orientations 3 and 4, and the exclusion of 4 reflections from orientation 2 on the refinement of the susceptibility tensor for **2**, we also decided to test the robustness of the refinement. To do this, instead of refining the susceptibility tensor from different combinations of data, we assume an atomic susceptibility tensor for Ho(III) in **2** and then calculate

the agreement with the data. This is done by deciding on the direction of the magnetic easy-axis and then building a set of orthogonal eigenvectors from this direction. Using the matrix diagonalization relation

$$\chi = VEV^T$$

where V is the matrix of eigenvectors, E is a diagonal matrix containing the eigenvalues, and χ is the simulated magnetic susceptibility tensor, we can represent the magnetic susceptibility tensor by any set of eigenvalues along these axes. The axes used as eigenvectors of the magnetic susceptibility tensor for our simulations are shown on top of the molecular structure of **2** in Figure S15.

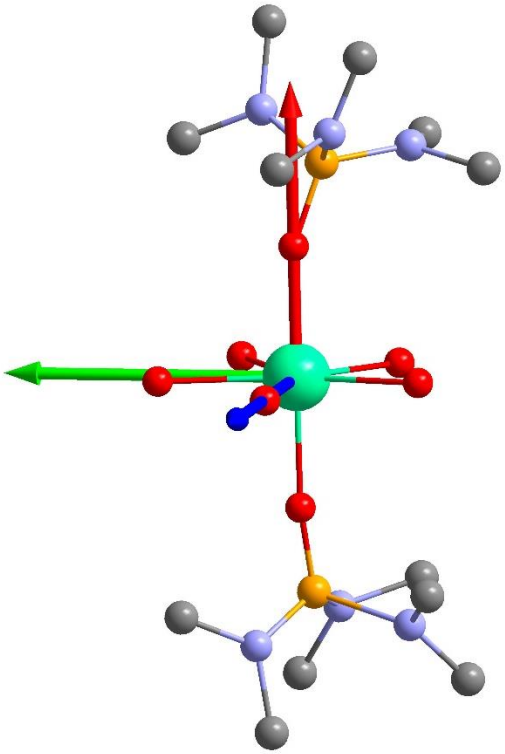

Figure S15. Axes used for the simulation of a susceptibility tensor to compare with the data for **2**.

When we simulate flipping ratios by using the eigenvalues obtained with model 3 together with the eigenvectors defined in Figure S15 and including all data from all 4 orientations (**model 4**), the agreement with the data worsens significantly. This shows that an easy-axis direction along the O-Ln-O-direction is not a viable model with this data. Similarly, using the eigenvalues obtained for **1** with the eigenvectors in Figure S15 and including all data for all 4 orientations (**model 5**) gives a marked increase in the χ^2-values. When a refinement is run using either model 4 or model 5 as a starting point, **model 3** is reproduced as expected. This increases our confidence in model 3 as being

a global minimum based on the full set of data measured for **2**. Plots of calculated vs. experimental flipping ratios for **model 3** are shown in Figure S15. The susceptibility tensors that correspond to models 2-5 are visualized on top of the molecular structure of **2** in Figure S17, and the agreement factors with the 4 orientations are shown in Table S11.

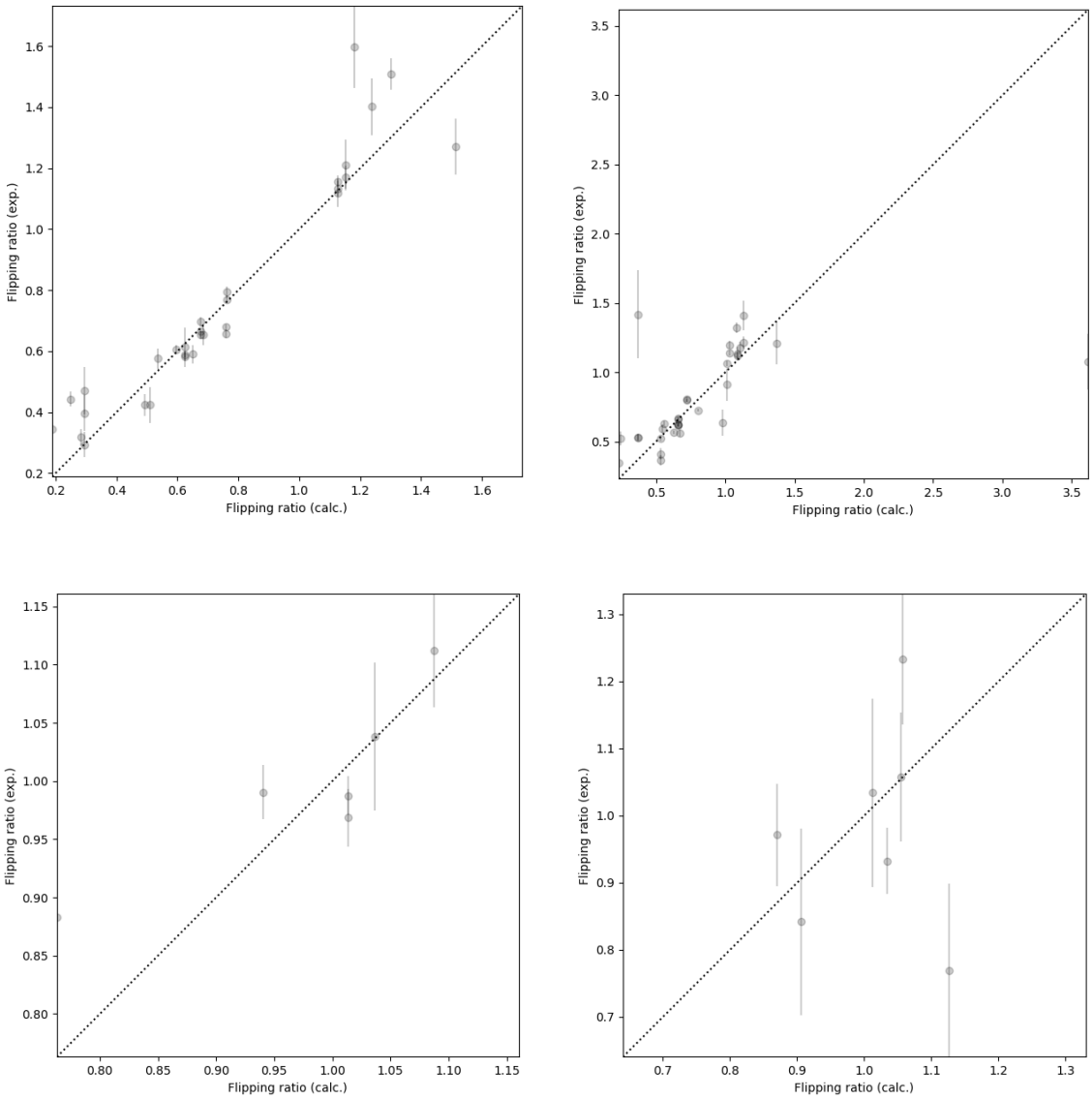

Figure S16. Agreement between model 3 and the data for **2**. The plots show calculated vs. experimental flipping ratios for orientation 1, 2, 3, and 4 from top left to bottom right respectively.

Table S11. Agreement factors between the 4 orientations measured for **2** and the 5 models described in the text.

	O1	O2	O3	O4	Overall
Model 1	10.64	25.33	N/A	N/A	18.21
Model 2	11.31	21.86	2.18	1.91	13.85
Model 3	10.71	25.62	2.84	2.44	15.74
Model 4	26.24	85.74	155.04	12.31	60.51
Model 5	19.69	78.02	0.34	0.76	41.46

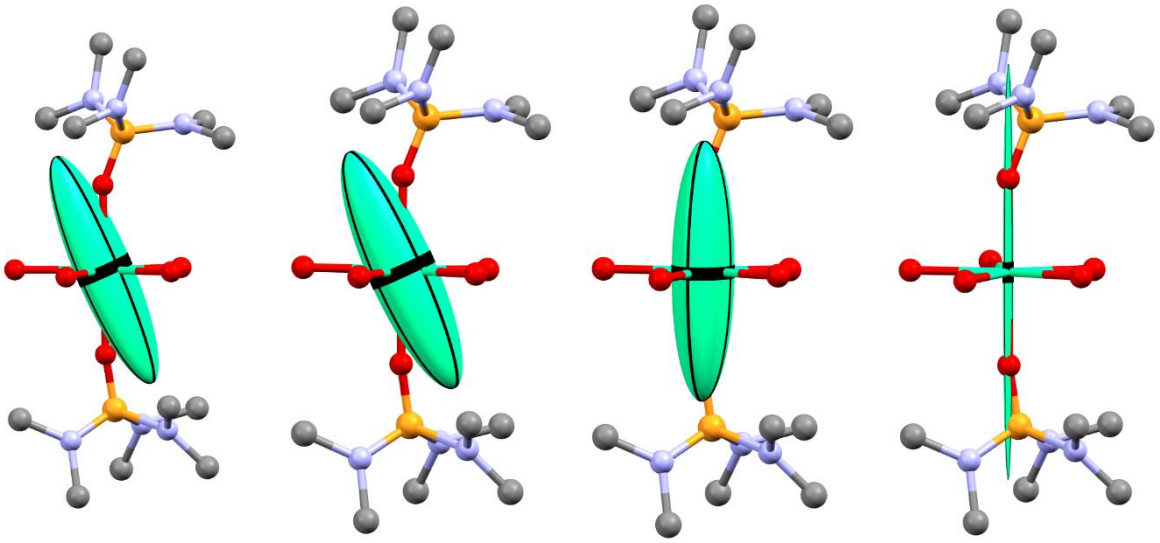

Figure S17. Visualization of models tested for their agreement against the experimental data. Models 2, 3, 4, and 5 are described in the text and presented from left to right.

7. References

1. G. Sheldrick, *Acta Crystallogr. Sect. A*, 2015, **71**, 3-8.
2. G. Sheldrick, *Acta Crystallogr. Sect. C*, 2015, **71**, 3-8.
3. O. V. Dolomanov, L. J. Bourhis, R. J. Gildea, J. A. K. Howard and H. Puschmann, *J. Appl. Crystallogr.*, 2009, **42**, 339-341.
4. M. Pinsky and D. Avnir, *Inorg. Chem.*, 1998, **37**, 5575-5582.
5. D. Casanova, P. Alemany, J. M. Bofill and S. Alvarez, *Chem. Eur. J.*, 2003, **9**, 1281-1295.
6. D. Casanova, J. Cirera, M. Llunell, P. Alemany, D. Avnir and S. Alvarez, *Journal of the American Chemical Society*, 2004, **126**, 1755-1763.
7. D. Gatteschi, R. Sessoli and J. Villain, *Molecular nanomagnets*, Oxford University Press, Oxford ; New York, 2006.
8. I. Fdez. Galván, M. Vacher, A. Alavi, C. Angeli, F. Aquilante, J. Autschbach, J. J. Bao, S. I. Bokarev, N. A. Bogdanov, R. K. Carlson, L. F. Chibotaru, J. Creutzberg, N. Dattani, M. G. Delcey, S. S. Dong, A. Dreuw, L. Freitag, L. M. Frutos, L. Gagliardi, F. Gendron, A. Giussani, L. González, G. Grell, M. Guo, C. E. Hoyer, M. Johansson, S. Keller, S. Knecht, G. Kovačević, E. Källman, G. Li Manni, M. Lundberg, Y. Ma, S. Mai, J. P. Malhado, P. Å. Malmqvist, P. Marquetand, S. A. Mewes, J. Norell, M. Olivucci, M. Oppel, Q. M. Phung, K. Pierloot, F. Plasser, M. Reiher, A. M. Sand, I. Schapiro, P. Sharma, C. J. Stein, L. K. Sørensen, D. G. Truhlar, M. Ugandi, L. Ungur, A. Valentini, S. Vancoillie, V. Veryazov, O. Weser, T. A. Wesołowski, P.-O. Widmark, S. Wouters, A. Zech, J. P. Zobel and R. Lindh, *Journal of Chemical Theory and Computation*, 2019, **15**, 5925-5964.
9. F. Aquilante, J. Autschbach, A. Baiardi, S. Battaglia, V. A. Borin, L. F. Chibotaru, I. Conti, L. De Vico, M. Delcey, I. Fdez. Galván, N. Ferré, L. Freitag, M. Garavelli, X. Gong, S. Knecht, E. D. Larsson, R. Lindh, M. Lundberg, P. Å. Malmqvist, A. Nenov, J. Norell, M. Odelius, M. Olivucci, T. B. Pedersen, L. Pedraza-González, Q. M. Phung, K. Pierloot, M. Reiher, I. Schapiro, J. Segarra-Martí, F. Segatta, L. Seijo, S. Sen, D.-C. Sergentu, C. J. Stein, L. Ungur, M. Vacher, A. Valentini and V. Veryazov, *The Journal of Chemical Physics*, 2020, **152**, 214117.
10. E. A. Klahn, C. Gao, B. Gillon, A. Gukasov, X. Fabrèges, R. O. Piltz, S.-D. Jiang and J. Overgaard, *Chemistry - A European Journal*, 2018, **24**, 16576-16581.
11. Y. Dong, P. Yan, X. Zou and G. Li, *Inorg. Chem. Front.*, 2015, **2**, 827-836.
12. S. Vaidya, S. K. Singh, P. Shukla, K. Ansari, G. Rajaraman and M. Shanmugam, *Chemistry – A European Journal*, 2017, **23**, 9546-9559.
13. J. Overgaard et al., in preparation
14. A. E. Whitten and M. A. Spackman, *Acta Crystallographica Section B*, 2006, **62**, 875-888.
15. J. C. Matthewman, P. Thompson and P. J. Brown, *J. Appl. Crystallogr.*, 1982, **15**, 167-173.
16. F. H. Allen and I. J. Bruno, *Acta Crystallographica Section B*, 2010, **66**, 380-386.
17. F. Guégan, J. Jung, B. Le Guennic, F. Riobé, O. Maury, B. Gillon, J.-F. Jacquot, Y. Guyot, C. Morell and D. Luneau, *Inorg. Chem. Front.*, 2019, **6**, 3152-3157.